frontiers | Frontiers in Earth Science

TYPE Original Research
PUBLISHED 05 January 2023
DOI 10.3389/feart.2022.1118079

OPEN ACCESS

EDITED BY
Yefei Ren,
Institute of Engineering Mechanics, China Earthquake Administration, China

REVIEWED BY
Weibing Gong,
University of California, Berkeley, United States
Ning Zhang,
Anhui Jianzhu University, China

*CORRESPONDENCE
Zhenghua Zhou,
bjsmoc@163.com

SPECIALTY SECTION
This article was submitted to Structural Geology and Tectonics, a section of the journal Frontiers in Earth Science

RECEIVED 07 December 2022
ACCEPTED 20 December 2022
PUBLISHED 05 January 2023

CITATION
Du L, Jin L and Zhou Z (2023), Analysis of the seismic effects of the local slope site of Longtoushan market town in Ludian Ms6.5 earthquake.
Front. Earth Sci. 10:1118079.
doi: 10.3389/feart.2022.1118079

Analysis of the seismic effects of the local slope site of Longtoushan market town in Ludian Ms6.5 earthquake

Liting Du[1], Liguo Jin[2] and Zhenghua Zhou[1]*

[1]College of Transportation Engineering, Nanjing Tech University, Nanjing, China, [2]Institute of Geophysics, China Earthquake Administration, Beijing, China

In the Ludian Ms6.5 earthquake (Yunnan, China), Longtoushan market town and its vicinity showed significant differences in earthquake damage. To explain this phenomenon, this paper discusses the local engineering geological conditions, local topographic effects, and seismic response of the soil layer in Longtoushan market town. The results show that complex topography and varied engineering geological conditions will lead to significant differences in ground motion, and then lead to significant differences in building earthquake damage. Slope topography has an obvious influence on ground motion. From the foot of the slope to the top of the slope, the degree of influence gradually increases, and the influence in different directions is different, as shown: the closer to the top of the slope, the more significant the difference. This indicates that the serious damage to buildings built on the slope is caused by the amplification effect of local terrain and the differential effect of ground motion. Although the site belongs to Class II site, the near-surface geotechnical properties and their combination characteristics, the physical state and thickness of the overlying soil layer, the variation characteristics of shear wave velocity, the non-linear dynamic characteristics of the soil, and other factors play a decisive role in the amplification degree of ground motion. The significant difference in ground motion on the surface of the slope site leads to a significant difference in seismic damage to buildings on the site. The covering soil layer has a significant effect on the acceleration response spectrum. The conclusions obtained in this paper can provide a scientific basis for the site selection of engineering construction and seismic design of building structures.

KEYWORDS

ground motion, site effect, local topography, response spectrum, ground pulsation

1 Introduction

China has been hit by several destructive earthquakes since 2000, causing heavy casualties and economic losses. For example, the Wenchuan Ms8.0 earthquake in 2008 caused more than 100,000 casualties and hundreds of billions of direct economic losses (Peng et al., 2011). In 2010, the Yushu Ms7.1 earthquake in Qinghai Province killed more than 2000 people (Ni et al., 2010). The Lushan Ms7.0 earthquake in Sichuan Province in 2013 caused hundreds of casualties (Li et al., 2013). The Jinggu Ms6.6 earthquake in Yunnan Province in 2014 also caused hundreds of casualties and economic losses of 5 billion yuan (Jia et al., 2016). Ludian Ms6.5 earthquake in Yunnan Province on 3 August 2014, caused 617 deaths, 112 missing, and 3,143 injured, and the direct

economic losses is 23.578 billion yuan (Hao et al., 2016). In the Ludian earthquake, the seismic intensity of Longtoushan market town was IX, which caused serious building damages, as shown in Figure 1.

In the Ludian earthquake, the strong-motion seismograph located in the Bureau of Finance of Longtoushan Market Town recorded a maximum acceleration value of 949 cm/s^2 in the EW direction, which is the largest peak ground acceleration (PGA) recorded in the meizoseismal area in the mainland of China so far (Cui et al., 2014). The investigation of the earthquake damage in the meizoseismal area shows that there is a large difference in the earthquake damage to buildings in Longtoushan Market Town, which is shown as "moderate earthquake but great disaster". The study of the abnormal earthquake damage phenomenon is helpful to reveal the mechanism of the abnormal earthquake damage, which has important reference value for the revision of the seismic design code of buildings and the site selection of construction projects.

Earthquake magnitude, propagation path, and local site conditions are the main factors affecting earthquake damage (Mayoral et al., 2019; Jin et al., 2020; Pamuk and Ozer., 2020). In the case of the Ludian earthquake, a mere Ms6.5 earthquake would not have been enough to cause such severe damage to Longtoushan Market Town. The only possible reason for the significant difference in earthquake damage, under the condition of a similar transmission path, is that the local site conditions have a significant impact on earthquake damage.

Local site conditions have a significant influence on earthquake damage to buildings (Panzera et al., 2018; Brando et al., 2020; Cetin et al., 2022; Huang et al., 2022). Borcherd et al. (1976) analyzed the San Francisco earthquake in 1906 and found that the earthquake damage to buildings located on bedrock or the hard site was light, while the earthquake damage to buildings located on soft ground was heavy. They pointed out that the site conditions have an important influence on earthquake damage. Subsequent earthquakes also show that site conditions have a significant impact on building earthquake damage (Estrella et al., 2003). For example, the Mexico earthquake in 1985, the Jiji earthquake in Taiwan in 1999 (Wang et al., 2002), and the Wenchuan earthquake in Sichuan in 2008 (Bo et al., 2009) all confirmed this conclusion. In addition, the influence of local terrain on building earthquake damage is mainly reflected in the amplification of local terrain on ground motion and the non-uniformity of spatial distribution (Geli et al., 1988; Çelebi et al., 1991; Shiann-Jong et al., 2009; Sun et al., 2011; Yang et al., 2018). This shows that for buildings located on complex terrain, it is necessary to consider local topographic effects in site selection and seismic design of engineering structures to ensure their safety under earthquakes.

The detailed seismic damage investigation data, strong motion records, and engineering geological data of the Ludian earthquake provide abundant materials for the analysis of local ground motion effects in Longtoushan Market Town. This paper will study the ground motion effect of the local slope site in Longtoushan Market Town through the analysis of local geological conditions, local topographic effect and seismic response of the soil layer, and then reveal the mechanism of serious earthquake damage in Longtoushan Market Town, so as to provide the basis for land planning, the site selection for engineering construction and building seismic design in Longtoushan Market Town.

2 Engineering geological condition

The Ludian earthquake area is located in the south-central section of the south-north-trending seismic belt on the eastern margin of the Qinghai-Tibet Plateau. The geological structure here is very complex, mainly the NE- and NW- trending fault structures. The NE-trending fault is mainly the Zhaotong-Ludian fault, which consists of three secondary faults. The NW-trending fault is mainly the Baogunao-Xiaohe fault, which consists of several short faults. Longtoushan Market Town is just in the intersection area of the Zhaotong-Ludian fault and the Baogunao-Xiaohe fault (Pang et al., 2016).

According to the investigation of Ludian earthquake damage, the geomorphic features of Longtoushan market town are mainly structural erosion canyons and denudating landforms of low mountain mounds, among which Longquan River and Shaba River pass through the town. Longtoushan market town is located between the foot of the mountain and the Longquan River, and the construction site is mostly the gentle slope landform formed by the accumulation of rivers. The overlying soil layer of bedrock mainly includes medium compressible clay containing gravel, pebbled silty clay, gravel soil, pebble, silty clay, and so on. Such complex topography and changeable geological conditions will have a significant impact on

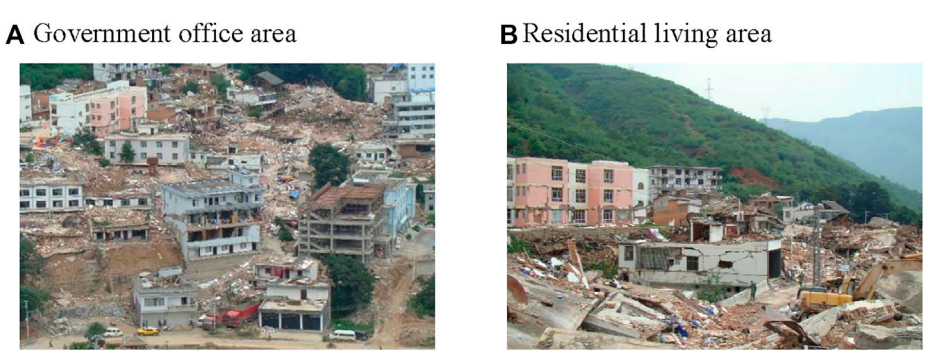

FIGURE 1
Earthquake damage in Longtoushan market town.

the ground motion, and then cause significant differences and zoning of earthquake damage.

3 Analysis of local topographic effect based on ground pulsation

The houses in Longtoushan market town are mainly built along the slope, and some of them are seriously damaged by the earthquake, as shown in Figure 2A. The methods of studying local topographic effects mainly include the analytical method, numerical simulation, and experimental study (physical model test and site observation). With the improvement of instrument observation accuracy and resolution, site observation, especially ground pulsation observation, has been widely used in the study of local topographic seismic effects. The research on the dynamic characteristics of a site based on ground pulsation (Nurwidyanto et al., 2021; Molnar et al., 2022) began in the 1960s, and the HVSR spectral ratio method proposed by Nakamura et al. (Pandey et al., 2018), has been the most widely used.

To analyze the amplification effect of the slope topography on ground motion in Longtoushan market town, the author takes the west slope of the family planning service station of Longtoushan Market Town as the observation object and carries out ground pulsation observation. The slope has an angle of about 18°. A total of six observation points were laid for the slope topography, as shown in Figures 2B, C. The instrument used in the field test is the ETNA2 accelerometer. The instrument has a built-in EpiSensor force-balance accelerometer, which can simultaneously record two horizontal and vertical acceleration time-histories at the observation point. ETNA2 accelerometer has a GPS time calibration function and has two modes of continuous recording and trigger recording. The sampling rate was 200 sps.

Through the observation of ground pulsation at six points, a total of about 3,000 s of ground pulsation has been recorded. After baseline correction, digital filtering, and segmental superposition and averaging of ground pulsation records, the time-history records that can be used for final analysis are obtained. Then Fourier transform is applied to the ground pulsation records after processing. Based on the transfer function method (reference point spectral ratio method) (Haghshenas et al., 2008), the two horizontal spectral ratio peaks of the 5 observation points (P_2-P_6) on the slope relative to the point P_1 at the slope foot and their corresponding frequencies can be obtained through calculation, as shown in Figure 3. The calculation results are shown in Table 1.

It can be seen from Table 1 that, the ratios between the peaks of the spectral ratio of the observation point (P_2-P_6) on the slope and that of the observation point P_1 are all greater than 1. From the foot of the slope to the top, the peaks of the spectral ratio become larger. The peak of the spectral ratio at the slope top (point P_6) is the largest, with the EW direction being 2.835 and the NS direction being 8.422. The frequencies corresponding to the peaks of the spectral ratio are also different. The frequency corresponding to the peak of the EW direction is always larger than that of the NS direction. The frequency range corresponding to the peak of the EW direction is 5.4 ~ 6.0 Hz, and the NS direction is 4.6 ~ 5.4 Hz. The peaks of the spectral ratio of the NS direction are always larger than that of the EW direction. The closer to the top of the slope, the more significant the difference in the spectral ratio peak.

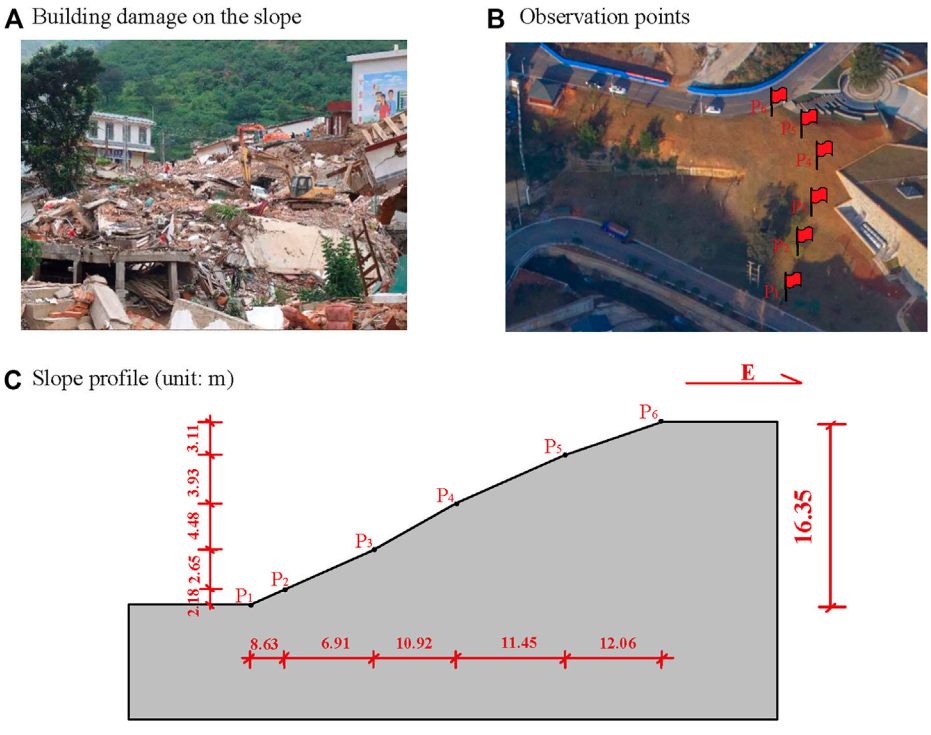

FIGURE 2
Building damage and observation point for ground pulsation on the slope site in Longtoushan Market Town.

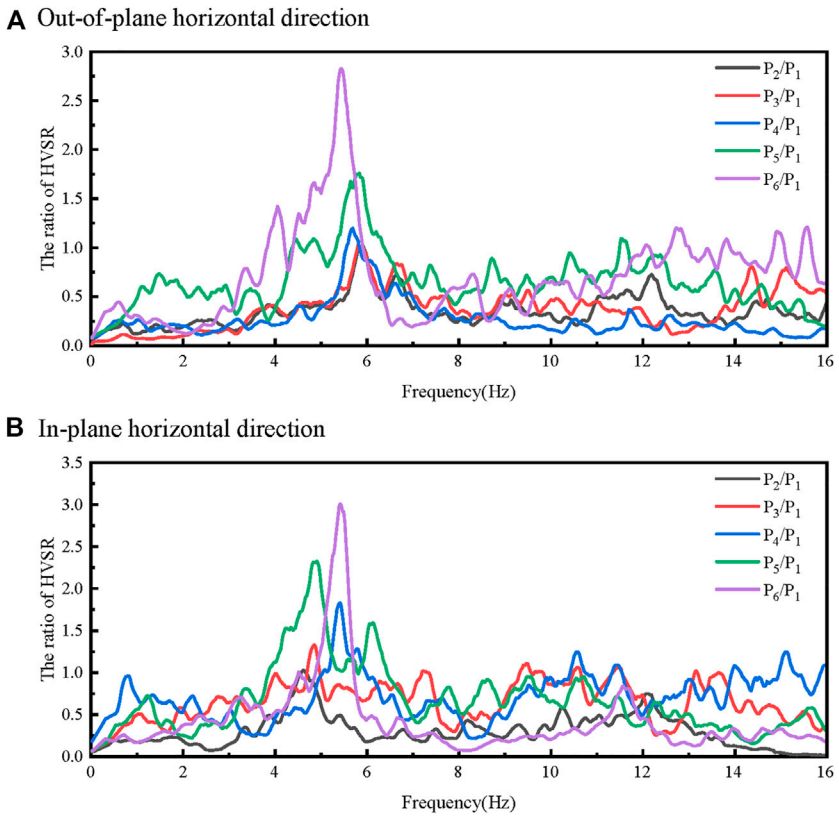

FIGURE 3
The ratio of HVSR between the observation points P_2–P_6 and P_1.

TABLE 1 Spectrum ratio of observation points on the slope.

Measuring point	Direction	Frequency of spectrum ratio (Hz)	Spectral peak value
P_2	EW	6.0	1.005
	NS	4.6	1.026
P_3	EW	5.8	1.044
	NS	4.9	1.330
P_4	EW	5.7	1.203
	NS	5.4	1.825
P_5	EW	5.8	1.760
	NS	4.9	2.332
P_6	EW	5.4	2.835
	NS	5.4	8.422

It can be seen that the slope site has a significant amplification effect on ground motion. The amplification effect is different from the foot of the slope to the top of the slope, and the top of the slope has the largest amplification effect. Meanwhile, the amplification effect in the slope site also has a significant difference in different directions. It can be inferred that the serious damage to buildings built on slopes is caused by the amplification effect of local terrain and the difference in ground motion.

To confirm the conclusion obtained by the ground pulsation test, the finite element method is used to analyze the dynamic characteristics of the slope topography. Based on ABAQUS® software, the numerical calculation model was established, as

shown in Figure 4A. According to Liao et al. (1984), the model mesh size is determined by 1/10 ~ 1/8 of the wavelength that corresponds to the cutoff frequency. To ensure the accuracy and efficiency of calculation, the size of the grid is taken as 1 m × 1 m. In this paper, two conditions are considered: 1) the soil is the completely weathered rock, with a shear wave velocity of 300 m/s and Poisson's ratio of 0.35; ② the soil is the bedrock, with shear wave velocity of 500 m/s and Poisson's ratio is 0.25. In both cases, the soil is assumed to be elastic homogeneous isotropic, with mass density of 2,350 kg/m^3. For eliminating the influence of artificial boundaries, the viscoelastic artificial boundaries were applied to the bottom and the two side boundaries of the model (Liu et al., 2020). The input is an approximate δ-pulse incident vertically at the bottom boundary (Liao et al., 1981; Hao et al., 2014). The approximate δ-pulse and its Fourier amplitude spectrum are shown in Figure 4B, and the cutoff frequency of the pulse is 12 Hz.

The horizontal and vertical displacement time histories of each observation point on the slope terrain are shown in Figures 5A, B. The authors determined the dynamic amplification coefficient of the observation point relative to the input pulse (the ratio of the peak displacement of the observation points to that of the input pulse), and obtained the variation trend of the dynamic amplification coefficient of the site along the slope terrain, as shown in Figure 5C. As can be seen from the figure, as the observation point gradually rises along the slope, the dynamic amplification coefficient gradually increases, and the observation point at the top of the slope has the largest dynamic amplification coefficient. The dynamic amplification coefficients of the observation points A_1–A_6 and A_{12}–A_{16} are close to the free-field results, which indicates that the influence of the slope can be ignored when the distance from the slope terrain is more than 2 times the slope height. It can be seen from Table 1 and Figure 5 that, the numerical simulation is basically consistent with the pulsation test at the top and foot of the slope, thus confirming each other.

4 Analysis of earthquake response of slope site

Based on the boreholes (DZK1-DZK6) data and experimental data corresponding to the six observation points, the one-dimensional equivalent linearization method (Astroza et al., 2017; Rui et al., 2021) is adopted to calculate the site seismic response at the six observation points. Through this calculation, the influence of the near-surface covering soil layer on ground motion is analyzed, and then the earthquake damage to buildings is discussed. Tables 2, 3 respectively give the soil layer information and the dynamic characteristic parameters of the soil at the observation points.

According to the data shown in Table 2, the equivalent shear wave velocity of each borehole (DZK1-DZK6) at 20 m depth is 273.5, 270.3, 373.4, 347.4, 401.9, and 254.6 m/s respectively; the thickness of the covered soil layers is 26.0, 59.1, 24.3, 59.0, and 28.3/18.7 m, respectively. According to Code for Seismic Design of Buildings (GB 50011–2010) in China, the slope site belongs to Class II building site.

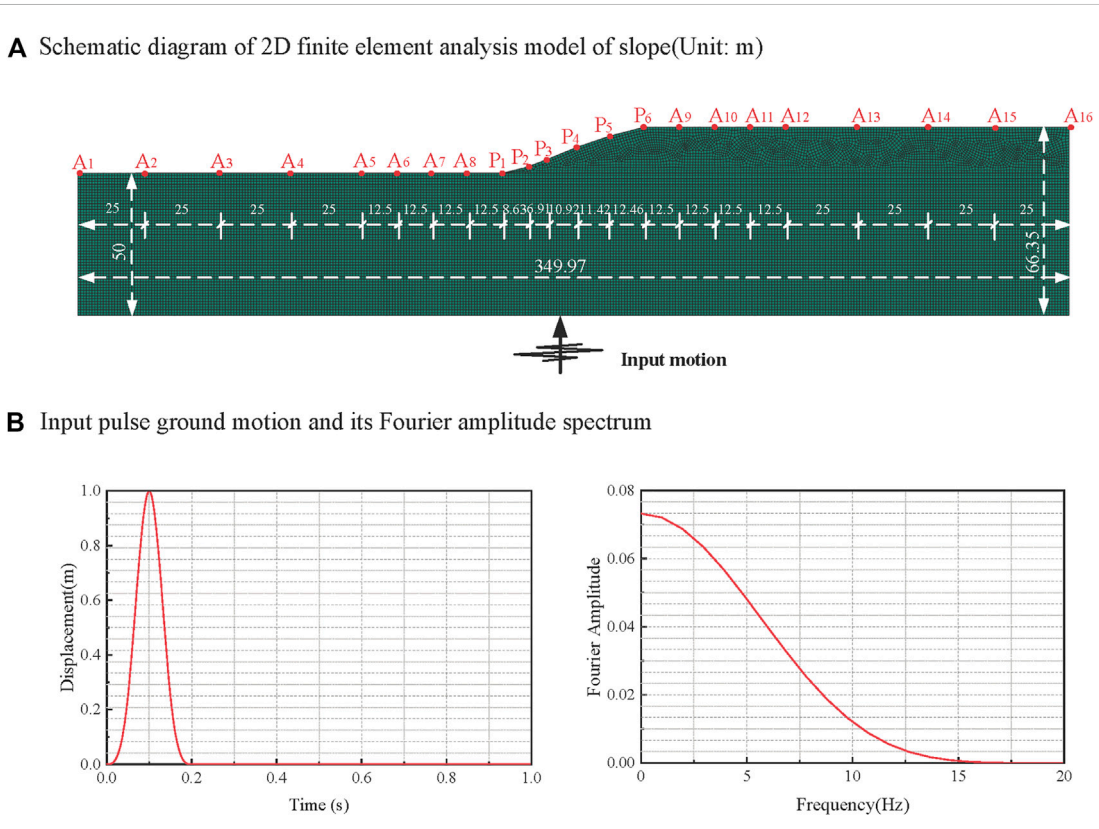

FIGURE 4
Finite element model of the slope site and the input pulse.

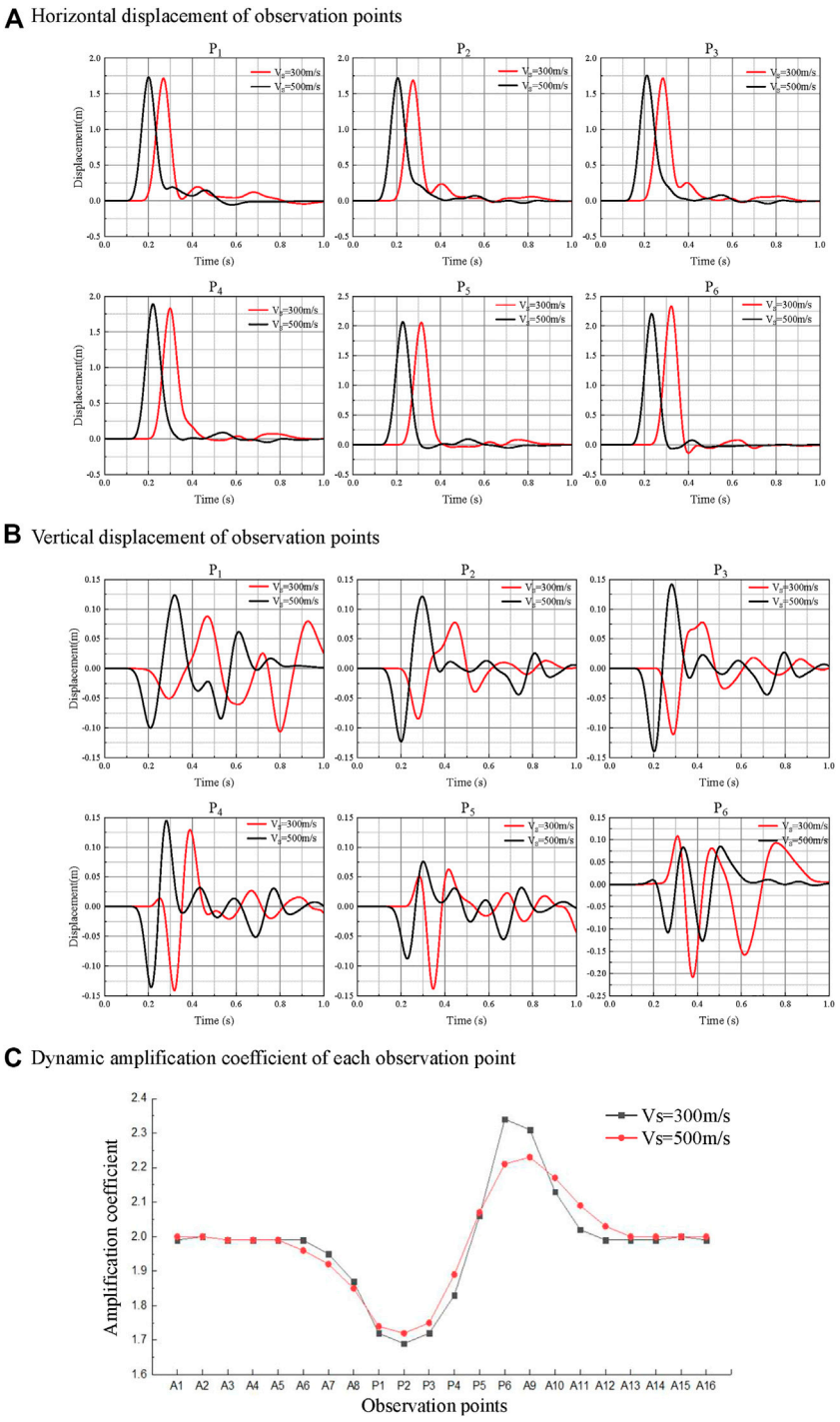

FIGURE 5
Calculation result of the finite element model of the 2D slope site.

In the Ludian Ms6.5 earthquake, there was a strong motion observation station (53LLT) near the DZK1 borehole, which is less than 10 km away from the epicenter (Cui et al., 2014; Ji et al., 2014). The station recorded the strong motion time-history in the EW direction, NS direction, and vertical direction, with the peak acceleration of 949, 706, and 504 cm/s^2, respectively. These are the maximum acceleration records during the Ludian earthquake. Therefore, in the one-dimensional seismic response analysis of the site, we multiply the EW-direction acceleration record by the reduction coefficient of 0.5 to obtain the input ground motion from the base. The input ground motion and its response spectrum are shown in Figure 6. It can be seen that the input ground motion has a wide frequency band, and the characteristic period is about 0.7 s, rich in long-period components.

By calculating the horizontal seismic response of each borehole, the horizontal ground acceleration time-history and response

TABLE 2 Information of the soil layers corresponding to the boreholes.

DZK	Layer	Soil	Depth (m)	Height (m)	Shear wave velocity (m/s)	Density (t/m^3)	Soil type number
DZK1	1	Miscellaneous fill	3.2	3.2	185.0	1.87	24
	2	Round gravel	11.8	8.6	281.0	2.25	1
	3	Round gravel	19.1	7.3	327.0	2.25	2
	4	Gravelly sand	23.0	3.9	310.0	2.15	3
	5	Gravelly sand	26.0	3.0	310.0	2.15	4
	6	Computational base	—	—	758.0	2.50	26
DZK2	1	Plain fill	1.2	1.2	201.0	1.72	24
	2	Round gravel	4.5	3.3	277.0	2.25	12
	3	Silt	5.1	0.6	270.0	1.96	5
	4	Round gravel	7.0	1.9	328.0	2.25	1
	5	Boulder	7.8	0.8	542.0	2.45	26
	6	Weathered quartz sand	15.6	7.8	453.0	2.23	6
	7	Fault breccia	18.0	2.4	521.0	2.45	26
	8	Weathered quartz sand	59.1	41.1	496.0	2.23	6
	9	Computational base	—	—	586.0	2.50	26
DZK3	1	Miscellaneous fill	1.2	1.2	190.0	1.87	24
	2	Round gravel	9.9	8.7	379.0	2.25	1
	3	Gravel silty clay	12.1	2.2	332.0	1.94	7
	4	Dust	13.5	1.4	445.0	2.10	25
	5	Broken stone	16.0	2.5	472.0	2.10	25
	6	Gravelly sand	21.2	5.2	434.0	2.15	3
	7	Gravel silty clay	24.3	3.1	431.0	1.99	9
	8	Computational base	—	—	539.0	2.50	26
DZK4	1	Miscellaneous fill	3.2	3.2	211.0	1.87	24
	2	Pebble	4.7	1.5	432.0	2.10	25
	3	Round gravel	9.8	5.1	417.0	2.25	1
	4	Gravel silty clay	12.5	2.7	375.0	1.94	7
	5	silt	13.2	0.7	379.0	1.96	5
	6	Gravel silty clay	18.0	4.8	385.0	1.97	8
	7	Gravel silty clay	24.0	6.0	385.0	1.99	9
	8	Gravel silty clay	30.1	6.1	385.0	2.00	10
	9	Weathered limestone	59.0	28.9	462.0	2.20	11
	10	Computational base	—	—	510.0	2.50	26
DZK5	1	Plain fill	1.0	1.0	281.0	1.72	24
	2	Round gravel	6.7	5.7	391.0	2.25	12
	3	Pebble	7.7	1.0	440.0	2.10	25
	4	Round gravel	9.5	1.8	419.0	2.25	13
	5	Round gravel	11.5	2.0	419.0	2.25	14
	6	Round gravel	15.0	3.5	419.0	2.25	15

(Continued on following page)

TABLE 2 (*Continued*) Information of the soil layers corresponding to the boreholes.

DZK	Layer	Soil	Depth (m)	Height (m)	Shear wave velocity (m/s)	Density (t/m^3)	Soil type number
	7	Round gravel	21.8	6.8	419.0	2.25	16
	8	Weathered limestone	22.5	0.7	545.0	2.20	11
	9	Fault gouge	23.1	0.6	392.0	1.86	17
	10	Moderately limestone	27.5	4.4	759.0	2.50	26
	11	Fault gouge	28.3	0.8	392.0	1.86	17
	12	Computational base	—	—	759.0	2.50	26
DZK6	1	Plain fill	1.0	1.0	165.0	1.72	24
	2	Silty clay	4.4	3.4	217.0	1.92	18
	3	Clay	6.5	2.1	213.0	1.86	19
	4	Gravel silty clay	9.2	2.7	234.0	1.86	20
	5	Gravelly sand	10.8	1.6	274.0	2.15	3
	6	Clay	11.6	0.8	321.0	1.86	19
	7	Gravelly sand	13.7	2.1	259.0	2.15	3
	8	Silty clay	15.5	1.8	360.0	2.03	21
	9	Silty clay	18.7	3.2	360.0	1.85	22
	10	Weathered limestone	26.5	7.8	703.0	2.20	23
	11	Computational base	—	—	804.0	2.50	26

spectrum at each borehole can be obtained. The peak of horizontal acceleration of the ground surface at the location of each borehole and the ratios with the peak of input motion (Peak acceleration ratio) are shown in Figure 7A. The response spectrum (damping ratio 5%) for the boreholes is shown in Figure 7B.

It can be seen from Figure 7A that, there are significant differences in peak values of ground surface acceleration at different observation points. DZK6 borehole has the maximum peak value of ground acceleration, and the ratio between it and the peak recorded (input motion shown in Figure 6) by the 53LLT observation station is 1.81. The peaks of ground surface acceleration corresponding to DZK1, DZK3 and DZK5 boreholes are similar, and all of them are slightly higher than those recorded by the 53LLT observation station, with the ratios of peak acceleration are 1.11, 1.16, and 1.12, respectively. Similarly, the ratios of peak ground surface acceleration corresponding to DZK2 and DZK4 boreholes are 0.78 and 0.47 respectively, which is close to the peak acceleration recorded by the 53LLT observation station. It should be noted that the DZK4 borehole has the lowest peak ground acceleration which is smaller than the peak of the input ground motion. The results show that the ground motion amplification effect at DZK1, DZK3, DZK5 and DZK6 boreholes is higher than that of 53LLT observation station, especially at the location of the DZK6 borehole. However, the ground motions at DZK2 and DZK4 boreholes have different degrees of attenuation, and the attenuation at the position of the DZK4 borehole is the most obvious. It can be seen that the amplification effect of the site on ground motion is jointly determined by the properties of the rock and soil near the ground surface and their composition, the physical state and thickness of the overlying soil, the velocity variation characteristics, and the non-linear dynamic characteristics of the soil.

The response spectrum shown in Figure 7B demonstrates that the response spectra of the ground surface acceleration time-histories that correspond to different boreholes are also significantly different. The acceleration response spectra that correspond to DZK1, DZK3, and DZK5 boreholes are close to each other and close to that of the 53LLT observation station in the period range of 0.2–0.45 s and 1.4–20 s. The difference in the response spectrum of ground surface acceleration corresponding to DZK4 and DZK6 is obvious. When the period is less than 1.2 s, the response spectrum value of the DZK4 borehole is smaller than that of the 53LLT observation station, but it is similar for the rest of the period. For the DZK6 borehole, when the period is less than 0.9 s, the value of the response spectrum is larger than that of the 53LLT observation station but similar for the rest period. In addition, in the period range of 0.65–1.6 s, the response spectra corresponding to DZK1 and DZK5 boreholes are slightly higher than that of the 53LLT observation station. It can be seen that the soil layer close to the ground surface has a significant influence on the acceleration response spectrum, and it is period-dependent.

From the above analysis, it can be seen that although the engineering site corresponding to the six boreholes is Class II site, due to the differences in geotechnical properties and their combination characteristics, the physical state and layer thickness of the overlying soil layer, the change of shear wave velocity, and

TABLE 3 Dynamic non-linear parameters of different soil layers.

Soil type number	Soil	Modulus ratio	Shearing strain γ (10^{-4})							
		Damping ratio	0.05	0.1	0.5	1	5	10	50	100
1	Round gravel	G/G_{max}	0.9976	0.9952	0.9765	0.9541	0.8061	0.6752	0.2937	0.1721
		λ	0.0060	0.0093	0.0252	0.0382	0.0942	0.1301	0.2116	0.2337
2	Round gravel	G/G_{max}	0.9954	0.9909	0.9560	0.9157	0.6847	0.5206	0.1784	0.0980
		λ	0.0037	0.0063	0.0212	0.0351	0.0976	0.1350	0.2049	0.2203
3	Gravelly sand	G/G_{max}	0.9975	0.9950	0.9757	0.9526	0.8007	0.6676	0.2866	0.1673
		λ	0.0052	0.0082	0.0232	0.0361	0.0927	0.1298	0.2145	0.2374
4	Gravelly sand	G/G_{max}	0.9933	0.9868	0.9371	0.8817	0.5984	0.4270	0.1297	0.0693
		λ	0.0076	0.0123	0.0365	0.0569	0.1339	0.1717	0.2301	0.2412
5	Silt	G/G_{max}	0.9970	0.9940	0.9706	0.9429	0.7675	0.6227	0.2482	0.1417
		λ	0.0026	0.0043	0.0143	0.0237	0.0684	0.0985	0.1659	0.1834
6	Weathered sandstone	G/G_{max}	0.9938	0.9878	0.9416	0.8897	0.6173	0.4465	0.1389	0.0746
		λ	0.0010	0.0021	0.0112	0.0222	0.0833	0.1235	0.1977	0.2135
7	Gravel silty clay	G/G_{max}	0.9980	0.9960	0.9804	0.9616	0.8337	0.7148	0.3339	0.2004
		λ	0.0006	0.0012	0.0055	0.0105	0.0430	0.0722	0.1627	0.1939
8	Gravel silty clay	G/G_{max}	0.9937	0.9876	0.9408	0.8882	0.6137	0.4427	0.1371	0.0736
		λ	0.0005	0.0012	0.0077	0.0164	0.0711	0.1098	0.1844	0.2005
9	Gravel silty clay	G/G_{max}	0.9942	0.9885	0.9453	0.8962	0.6333	0.4633	0.1472	0.0795
		λ	0.0133	0.0196	0.0470	0.0673	0.1365	0.1690	0.2190	0.2286
10	Gravel silty clay	G/G_{max}	0.9968	0.9937	0.9692	0.9402	0.7586	0.6111	0.2392	0.1358
		λ	0.0066	0.0102	0.0275	0.0416	0.0998	0.1345	0.2049	0.2219
11	Weathered limestone	G/G_{max}	0.9862	0.9728	0.8772	0.7812	0.4166	0.2631	0.0666	0.0345
		λ	0.0083	0.0138	0.0431	0.0666	0.1397	0.1667	0.1993	0.2045
12	Round gravel	G/G_{max}	0.9872	0.9746	0.8849	0.7935	0.4345	0.2776	0.0714	0.0370
		λ	0.0082	0.0136	0.0427	0.0663	0.1415	0.1702	0.2057	0.2114
13	Round gravel	G/G_{max}	0.9975	0.9950	0.9754	0.9520	0.7987	0.6648	0.2840	0.1655
		λ	0.0007	0.0014	0.0065	0.0124	0.0494	0.0807	0.1678	0.1944
14	Round gravel	G/G_{max}	0.9941	0.9833	0.9443	0.8945	0.6291	0.4589	0.1450	0.0782
		λ	0.0030	0.0053	0.0192	0.0323	0.0902	0.1229	0.1786	0.1900
15	Round gravel	G/G_{max}	0.9979	0.9959	0.9796	0.9601	0.8280	0.7065	0.3249	0.1940
		λ	0.0005	0.0011	0.0055	0.0110	0.0493	0.0854	0.2007	0.2407
16	Round gravel	G/G_{max}	0.9912	0.9826	0.9189	0.8499	0.5311	0.3615	0.1017	0.0536
		λ	0.0112	0.0174	0.0464	0.0686	0.1417	0.1725	0.2145	0.2217
17	Fault gouge	G/G_{max}	0.9956	0.9912	0.9575	0.9184	0.6924	0.5295	0.1837	0.1012
		λ	0.0033	0.0058	0.0207	0.0351	0.1030	0.1454	0.2273	0.2458
18	Silty clay	G/G_{max}	0.9988	0.9975	0.9878	0.9758	0.8897	0.8013	0.4465	0.2874
		λ	0.0025	0.0041	0.0124	0.0199	0.0570	0.0856	0.1742	0.2075
19	Clay	G/G_{max}	0.9982	0.9964	0.9821	0.9648	0.8458	0.7328	0.3542	0.2152
		λ	0.0005	0.0009	0.0047	0.0092	0.0412	0.0720	0.1760	0.2144

(Continued on following page)

TABLE 3 (*Continued*) Dynamic non-linear parameters of different soil layers.

Soil type number	Soil	Modulus ratio	Shearing strain γ (10^{-4})							
		Damping ratio	0.05	0.1	0.5	1	5	10	50	100
20	Gravel silty clay	G/G_{max}	0.9989	0.9978	0.9892	0.9787	0.9018	0.8211	0.4786	0.3146
		λ	0.0069	0.0101	0.0245	0.0358	0.0835	0.1164	0.2107	0.2453
21	Silty clay	G/G_{max}	0.9961	0.9922	0.9620	0.9268	0.7170	0.5589	0.2022	0.1125
		λ	0.0015	0.0027	0.0111	0.0200	0.0673	0.1002	0.1704	0.1875
22	Silty clay	G/G_{max}	0.9991	0.9982	0.9913	0.9828	0.9193	0.8507	0.5326	0.3630
		λ	0.0034	0.0052	0.0134	0.0201	0.0504	0.0726	0.1430	0.1719
23	Weathered limestone	G/G_{max}	0.9941	0.9883	0.9441	0.8940	0.6279	0.4576	0.1444	0.0778
		λ	0.0008	0.0018	0.0103	0.0211	0.0858	0.1307	0.2176	0.2366
24	Filling	G/G_{max}	0.960	0.950	0.800	0.700	0.300	0.200	0.150	0.100
		λ	0.025	0.028	0.030	0.035	0.080	0.100	0.110	0.120
25	Gravel/crushed stone	G/G_{max}	0.990	0.970	0.900	0.850	0.700	0.550	0.320	0.200
		λ	0.004	0.006	0.019	0.030	0.075	0.090	0.110	0.120
26	Bedrock	G/G_{max}	1.000	1.000	1.000	1.000	1.000	1.000	1.000	1.000
		λ	0.050	0.050	0.050	0.050	0.050	0.050	0.050	0.050

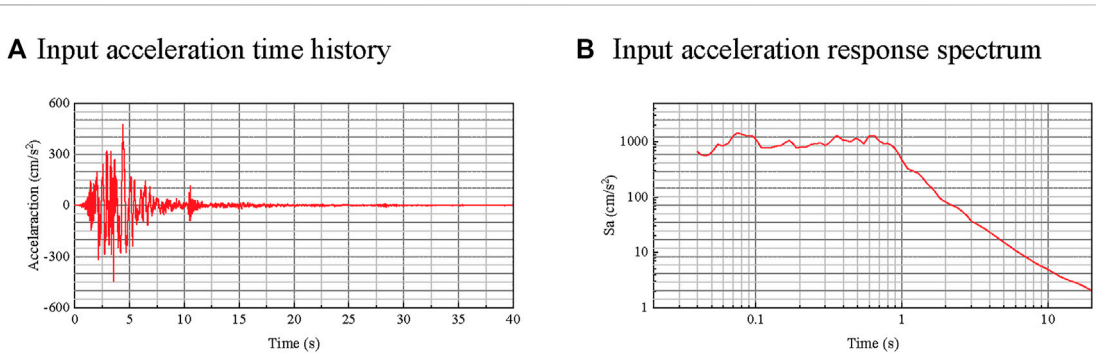

FIGURE 6
Input ground motion for site seismic response analysis and its response spectrum.

the dynamic non-linear characteristics of the soil, the amplification effect on the ground motion at different borehole position is significantly different, which will cause a significant difference in the seismic damage of the house at the location of different borehole.

Figure 8 shows the damage to the buildings located at different borehole positions. The locations of boreholes DZK1, DZK3, DZK5, and DZK6 respectively correspond to the 53LLTobservation station, the west side of the administration office area, the old block, and the living area. In these areas, the houses are more severely damaged. The DZK2 borehole is located on a middle school campus where the damage to the buildings is relatively light. The DZK4 borehole is located in a kindergarten where the main structure of the buildings has not been seriously damaged. The seismic response analysis of the site showed that the amplification effect on the ground motion at the positions of DZK1, DZK3, DZK5, and DZK6 boreholes is most significant compared with that at the location of the DZK4 borehole, while the amplification effect on the ground motion at the location of DZK2 borehole is relatively small. This feature is consistent with the actual earthquake damage, that is, where the amplification of ground motion is stronger, the damage to the building is heavier. This can show that the amplification effect of the site on the ground motion has a significant impact on building damage, and the more significant the amplification on ground motion, the more serious the building damage.

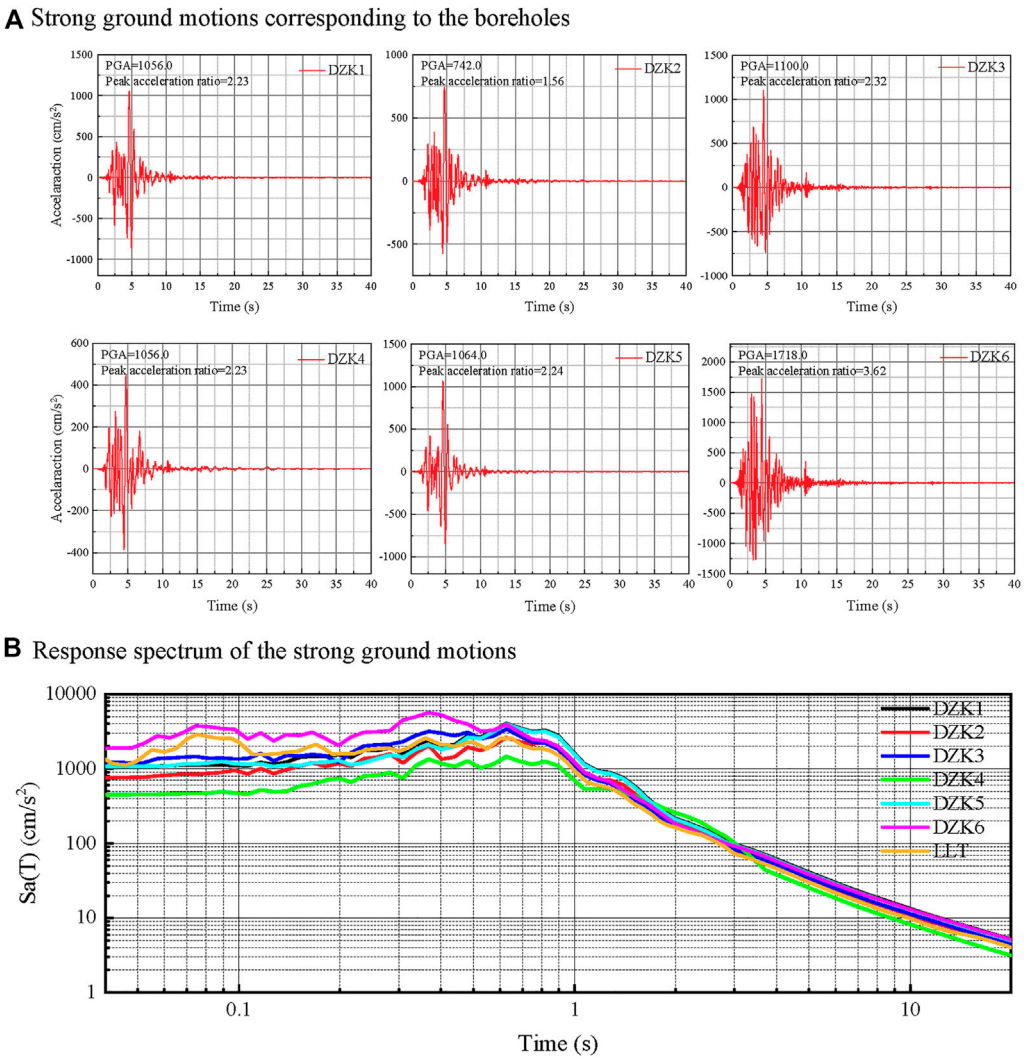

FIGURE 7
Site seismic response calculation based on one-dimensional equivalent linearization method.

FIGURE 8
Earthquake damage in Longtoushan Market Town.

5 Conclusion

In this paper, the amplification effect of the slope site on ground motion in Longtoushan Market Town is discussed through the analysis of local site engineering geological conditions, local topographic effects and seismic response analysis of the slope site, and its influence on building earthquake damage is further investigated. The main findings and conclusions are as follows:

1) Complex topography and variable engineering geological conditions will lead to significant differences in ground motion, which in turn will lead to significant differences in seismic damage to buildings. For slope sites, from the foot of the slope to the top of the slope, the amplification effect of the site on ground motion gradually becomes stronger. In different directions of the same location of the site, the site amplifies ground motion differently.
2) The strength of the amplification effect of the site on ground motion is determined by the properties of the rock and soil near the ground surface and their composition, the physical state and thickness of the overlying soil layer, the changes of shear wave speed, and the dynamic non-linear characteristics of the soil. This will lead to significant differences in ground motion amplification effects at different locations of the site, which in turn will lead to significant differences in the seismic damage of houses located at different locations on the site.
3) The soil layer close to the ground surface has a significant influence on the ground motion acceleration response spectrum, and it is period-dependent. The analysis of the site seismic response is consistent with the actual seismic damage investigation. The amplification effect of the site on the ground motion has a significant impact on building damage, and the more significant the amplification on ground motion, the more serious the building damage.

Data availability statement

The original contributions presented in the study are included in the article/supplementary material, further inquiries can be directed to the corresponding author.

Author contributions

LD: Validation, Formal analysis, Visualization. LJ: Conceptualization, Validation, Formal analysis, Data curation, Visualization, Writing—original draft—review and editing. ZZ: Software, Data curation, Supervision, Writing—review and editing.

Funding

This study is supported by the National Natural Science Foundation of China (Grant No. U2039208, U1839202).

Conflict of interest

The authors declare that the research was conducted in the absence of any commercial or financial relationships that could be construed as a potential conflict of interest.

Publisher's note

All claims expressed in this article are solely those of the authors and do not necessarily represent those of their affiliated organizations, or those of the publisher, the editors and the reviewers. Any product that may be evaluated in this article, or claim that may be made by its manufacturer, is not guaranteed or endorsed by the publisher.

References

Astroza, R., César., P., and Ochoa-Cornejo, F. (2017). Site response analysis using one-dimensional equivalent-linear method and bayesian filtering. *Comput. Geotechnics* 89, 43–54. doi:10.1016/j.compgeo.2017.04.004

Bo, J., Qi, W., and Liu, H. (2009). Abnormality of seismic intensity in hanyuan during wenchuan earthquake. *Earthq. Eng. Eng. Vib.* 29 (6), 53–64.

Borcherdt, R., and Gibbs, J. (1976). Effects of local geological conditions in the San Francisco Bay region on ground motions and the intensities of the 1906 earthquake. *Bull. Seismol. Soc. Am. (United States)* 66 (2), 467–500. doi:10.1785/bssa0660020467

Brando, G., Pagliaroli, A., Cocco, G., and Di, B. (2020). Site effects and damage scenarios: The case study of two historic centers following the 2016 central Italy earthquake. *Eng. Geol.* 272, 105647. doi:10.1016/j.enggeo.2020.105647

Çelebi, M. (1991). Topographical and geological amplification: Case studies and engineering implications. *Struct. Saf.* 10, 199–217. doi:10.1016/0167-4730(91)90015-2

Cetin, L., Kemal, O., Altun, S., Askan, A., Sezer, A., Kincal, C., et al. (2022). The site effects in izmir bay of october 30 2020, M7.0 samos earthquake. *Soil Dyn. Earthq. Eng.* 152, 107051. doi:10.1016/j.soildyn.2021.107051

Cui, J., Liu, Q., and Duan, J. (2014). Strong-motion recordings of MS6.5 ludian earthquake in yunnan in 2014 and their preliminary analysis. *J. Seismol. Res.* 37 (4), 542–548.

Estrella, H., and González, J. (2003). Spac: An alternative method to estimate earthquake site effects in Mexico city. *Geofísica Int.* 42 (2), 227–236. doi:10.22201/igeof.00167169p.2003.42.2.267

Geli, L., Bard, P. Y., and Jullien, B. (1988). The effect of topography on earthquake ground motion: A review and new results. *BSSA* 78 (1), 42–63. doi:10.1785/bssa0780010042

Haghshenas, E., Bard, P. Y., and Theodulidis, N., (2008). Empirical Evaluation of microtremor H/V spectral ratio. *Bull. Earthq. Eng.* 6 (01), 75–108. doi:10.1007/s10518-007-9058-x

Hao, C., Xie, Q., Dai, B., Zhang, H., and Chen, H. (2016). Seismic damage to structures in the Ms6.5 ludian earthquake. *Earthq. Eng. Eng. Vib.* 5 (01), 173–186. doi:10.1007/s11803-016-0314-4

Hao, M., Zhang, Y., and Zhao, F. (2021). Analysis of slope terrain effect on the properties of ground motion. *Technol. Earthq. Disaster Prev.* 16 (2), 229–236. (in Chinese).

Huang, Z. K., Zhang, D. M., Pitilakis, K., Tsinidis, G., Huang, H. W., Zhang, D., et al. (2022). Resilience assessment of tunnels: Framework and application for tunnels in alluvial deposits exposed to seismic hazard. *Soil Dyn. Earthq. Eng.* 162, 107456. doi:10.1016/j.soildyn.2022.107456

Ji, K., Wen, R., and Cui, J. (2014). Observation of strong motion and damage investigation for M_S6.5 ludian earthquake. *Technol. Earthq. Disaster Prev.* 9 (3), 325–339.

Jia, H., Chen, F., Fan, Y., and Pan, D. (2016). Comparison of two large earthquakes in China: The ms 6.6 yunnan jinggu earthquake and the ms 6.5 yunnan ludian earthquake in 2014. *Int. J. Disaster Risk Reduct.* 16, 99–107. doi:10.1016/j.ijdrr.2016.01.006

Jin, K., Lee, J., Lee, K., Kyung, J., and Kim, Y. (2020). Earthquake damage and related factors associated with the 2016 ML = 5.8 Gyeongju earthquake, southeast Korea. *Geosciences J.* 24 (2), 141–157. doi:10.1007/s12303-019-0024-9

Li, Z., Hou, J., and Li, Yang. (2013). Analysis on the characteristics of the MS7. 0 Lushan, Sichuan province, earthquake hazard on April 20, 2013. *Seismol. Geol.* 35 (2), 398–410.

Liao, Z. (1984). A finite element method for near-field wave motion in heterogeneous materials. *Earthq. Eng. Eng. Vib.* 4 (2), 1–14.

Liao, Z., Yang, B., and Yuan, Y. (1981). Effects of three-dimensional topography on earthquake ground motion. *Earthq. Eng. Eng. Vib.* 1 (1), 56–77.

Liu, J., Bao, X., and Tan, H. (2020). Seismic wave input method for soil-structure dynamic interaction analysis based on internal substructure. *China Civ. Eng. J.* 53 (8), 87–96. (in Chinese).

Mayoral, J., Asimaki, D., Tepalcapa, S., Wood, C., Roman-de, l., Hutchinson, T., et al. (2019). Site effects in Mexico City basin: Past and present. *Soil Dyn. Earthq. Eng.* 121, 369–382. doi:10.1016/j.soildyn.2019.02.028

Molnar, S., Sirohey, A., Assaf, J., Bard, P. Y., Castellaro, S., Cornou, C., et al. (2022). A review of the microtremor horizontal-to-vertical spectral ratio (MHVSR) method. *J. Seismol.* 26, 653–685. doi:10.1007/s10950-021-10062-9

Ni, S., Wang, W., and Li, L. (2010). The april 14th, 2010 Yushu earthquake, a devastating earthquake with foreshocks. *Sci. China (Earth Sci.* 53 (06), 791–793. doi:10.1007/s11430-010-0083-2

Nurwidyanto, M., Irhama, C., Zainuri, M., Yuliyanto, G., and Wirasatriya, A. (2021). Measurement of ground response of semarang coastal region risk of earthquakes by horizontal to vertical spectral ratio (HVSR) microtremor method. *J. Phys. Conf. Ser.* 1943 (1), 012033. doi:10.1088/1742-6596/1943/1/012033

Pamuk, E., and Ozer, C. (2020). The site effect investigation with using horizontal-to-vertical spectral ratio method on earthquake data, south of Turkey. *Geotectonics* 54 (4), 563–576. doi:10.1134/s001685212004010x

Pandey, A. K., Roy, P. N. S., Baidya, P. R., and Gupta, A. K. (2018). Estimation of current seismic hazard using Nakamura technique for the Northeast India. *Nat. Hazards* 93 (02), 1013–1027. doi:10.1007/s11069-018-3338-4

Pang, W., Yang, R., and Chen, J. (2016). High density resistivity exploration method for ludian MS6. 5 earthquake in area of longtoushan town in 2014. *J. Seismol. Res.* 39 (4), 622–629.

Panzera, F., Lombardo, G., Imposa, S., Grassi, S., Gresta, S., Catalano, S., et al. (2018). Correlation between earthquake damage and seismic site effects: The study case of lentini and carlentini, Italy. *Eng. Geol.* 240, 149–162. doi:10.1016/j.enggeo.2018.04.014

Peng, X., Liu, L., Li, X., and Sun, P. (2011). Study on correlation between building damage and strong motion parameters in wenchuan earthquake. *J. Basic Sci. Eng.* 19 (4), 574–582.

Rui, S., and Xiao, M. (2021). A holistic equivalent linear method for site response analysis. *Soil Dyn. Earthq. Eng.* 140 (1), 106476. doi:10.1016/j.soildyn.2020.106476

Shiann-Jong, L., Dimitri, K., Bor-Shouh, H., and Jeroen, T. (2009). Effects of topography on seismic-wave propagation: An example from northern taiwan. *BSSA* 99 (1), 314–325. doi:10.1785/0120080020

Sun, C., Ming, X., and Zhou, M. (2011). Influence of local topography on ground motion in mountain region of southern gansu province. *Northwest. Seismol. J.* 33 (4), 331–335.

Wang, G., Zhou, X., Zhang, P., and Igel, H. (2002). Characteristics of amplitude and duration for near fault strong ground motion from the 1999 chi-chi, taiwan earthquake. *Soil Dyn. Earthq. Eng.* 22 (1), 73–96. doi:10.1016/s0267-7261(01)00047-1

Yang, Y., Zhu, X., and Yang, Z. (2018). Analytic solution for diffraction of plane P waves by a circular alluvial valley in wedge-shaped space. *Technol. Earthq. Disaster Prev.* 13 (4), 810–821.